Front. Phys. China, 2010, 5(2): 150–160
DOI 10.1007/s11467-009-0076-9

REVIEW ARTICLE

Electronic structures of ternary iron arsenides $A\mathrm{Fe_2As_2}$ (A = Ba, Ca, or Sr)

Feng-jie MA (马锋杰)[1,2], **Zhong-yi LU** (卢仲毅)[1,†], **Tao XIANG** (向涛)[3,2,*]

[1] *Department of Physics, Renmin University of China, Beijing 100872, China*
[2] *Institute of Theoretical Physics, Chinese Academy of Sciences, Beijing 100190, China*
[3] *Institute of Physics, Chinese Academy of Sciences, Beijing 100190, China*
E-mail: †*zlu@ruc.edu.cn*, **txiang@aphy.iphy.ac.cn*

Received August 14, 2009; accepted September 21, 2009

We have studied the electronic and magnetic structures of the ternary iron arsenides $A\mathrm{Fe_2As_2}$ (A = Ba, Ca, or Sr) using the first-principles density functional theory. The ground states of these compounds are in a collinear antiferromagnetic order, resulting from the interplay between the nearest and the next-nearest neighbor superexchange antiferromagnetic interactions bridged by As 4p orbitals. The correction from the spin–orbit interaction to the electronic band structure is given. The pressure can reduce dramatically the magnetic moment and diminish the collinear antiferromagnetic order. Based on the calculations, we propose that the low energy dynamics of these materials can be described effectively by a t–J_H–J_1–J_2-type model [arXiv: 0806.3526v2, 2008].

Keywords iron arsenides superconductor, first-principles density functional theory, electronic structure, magnetic structure, superexchange antiferromagnetic interaction

PACS numbers 74.25.Ha, 74.25.Jb, 74.70.-b, 71.20.-b, 71.18.+y

Contents

1 Introduction

The recent discovery of superconductivity in LaFeAsO by partial substitution of O with F atoms below 26 K [2] has stimulated great interest on the investigation of the physical properties of iron-based pnictides. This type of quaternary compounds consists of alternative tetrahedral FeAs and LaO layers along the c-axis. The LaO layers act mainly as a charge reservoir. The superconducting pairing occurs in the FeAs layers. More recently, it was reported that the ternary iron-based arsenides $A\mathrm{Fe_2As_2}$ (A=Ba, Ca, or Sr) become superconducting upon hole or electron doping [3–6]. Similar as in LaFeAsO [7, 8], these ternary iron arsenides also exhibit a spin-density-wave-like anomaly and a structural transition from the tetragonal $I4/mmm$ to the orthorhombic $Fmmm$ group at some temperature between 140 K and 200 K [9, 10]. Furthermore, it was found that the high pressures can drive these undoped ternary iron arsenides to be superconducting [11–13].

To investigate the mechanism of superconductivity in these materials, it is commonly believed that one needs to understand first the electronic and magnetic structures of the parent compounds. It has been shown that

there is an essential similarity of electronic states near the Fermi level in AFe$_2$As$_2$ (A=Ba, Ca, or Sr) and LaFeAsO by studying the nonmagnetic state [1, 14]. Moreover, the density of states at the Fermi energy is only weakly doping dependent and the main effect of doping is a change in the relative sizes of the electron and hole Fermi surfaces [15].

In this paper, we report the electronic structures and magnetic orders and properties of AFe$_2$As$_2$ (A=Ba, Ca, or Sr) obtained from the first-principles electronic structure calculations. By comparison of the energy of the non-magnetic state with those of a number of magnetic ordered states, we find that, similar as in LaFeAsO, the ground state of AFe$_2$As$_2$ is in a collinear antiferromagnetic order. We have also studied the spin-orbit interaction and the pressure effect in these materials. The electronic and magnetic structure is found to be strongly affected by the pressure effect, but weakly by the spin-orbit interaction.

2 Computational approach

AFe$_2$As$_2$ (A=Ba, Ca, or Sr) takes the ThCr$_2$Si$_2$ type structure and an "A" layer plays a similar role as a LaO layer in LaFeAsO. Although AFe$_2$As$_2$ can be considered as a tetragonal crystal with two formula units included in the corresponding unit cell as shown in Fig. 1(a), its primitive unit cell is constructed by considering AFe$_2$As$_2$ as a triclinic crystal, in which only one formula unit cell is included as shown in Fig. 1(b). In the calculations, we adopted the primitive cell as calculation cell with the experimental lattice constants as the input parameters. In the calculation of the electronic structures of the non-magnetic, the ferromagnetic and the square antiferromagnetic Neel states, the $a \times a$ FeAs cell is taken as the base cell [shown in Fig. 1(c)]. In the calculation of the collinear antiferromagnetic state, the unit cell is doubled and the base cell is the $\sqrt{2}a \times \sqrt{2}a$ FeAs cell as shown in Fig. 1(c).

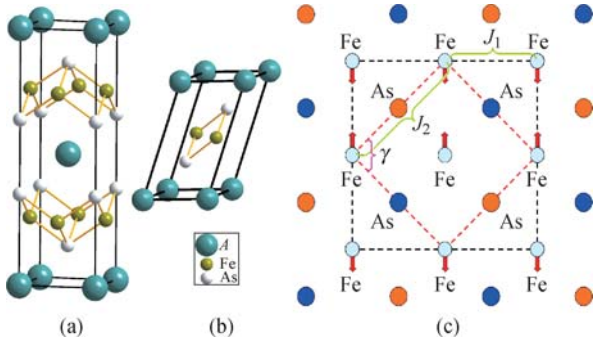

Fig. 1 AFe$_2$As$_2$ (A=Ba, Ca, or Sr): **(a)** a tetragonal unit cell containing two formula units; **(b)** a primitive unit cell containing one formula unit; **(c)** schematic top view of the FeAs layer. The small red dashed square is an $a \times a$ unit cell, while the large black dashed square is a $\sqrt{2}a \times \sqrt{2}a$ unit cell. The Fe spins in the collinear antiferromagnetic order are shown by arrows.

In our calculations the plane wave basis method was used [16]. We used the generalized gradient approximation (GGA) of Perdew–Burke–Ernzerhof [17] for the exchange-correlation potentials. The ultrasoft pseudopotentials [18] were used to model the electron–ion interactions. After the full convergence test, the kinetic energy cut-off and the charge density cut-off of the plane wave basis were chosen to be 600 eV and 4800 eV, respectively. The Gaussian broadening technique was used and a mesh of $16 \times 16 \times 8$ k-points were sampled for the Brillouin-zone integration. The internal atomic coordinates within a cell were determined by the energy minimization.

3 Results and analysis

3.1 Nonmagnetic state

We first studied the nonmagnetic state of the compound AFe$_2$As$_2$ (A = Ba, Sr, or Ca), which is the high temperature phase of these materials. The electronic band structure of this state also provides a reference for studying the low temperature magnetic phases. This can help us to understand the mechanism or the interactions that drive the magnetic phase transition and the related structural transition [19].

3.1.1 $BaFe_2As_2$

In our calculation, the experimental tetragonal crystal lattice parameters $a = b = 3.9625$ Å and $c = 13.0168$ Å [9] were adopted for BaFe$_2$As$_2$. Figures 2 and 3 show the calculated density of states (DOS) of BaFe$_2$As$_2$ in the nonmagnetic, square antiferromagnetic Neel, and collinear antiferromagnetic states, respectively. As revealed by Fig. 2(a), similar to LaFeAsO, the density of states of BaFe$_2$As$_2$ consists of mainly the Fe-3d states from –2 eV to 2 eV around the Fermi energy. Further analysis of the calculation [Fig. 3(a)] shows that the crystal field splitting of the Fe-3d orbitals is much smaller than the one in transition metal oxides. This is not very surprising since the electronegativity of As is much weaker than O. This suggests that the Fermi surface may have the contribution from all the Fe-3d orbitals.

The electronic band structure and the Fermi surface of BaFe$_2$As$_2$ in the nonmagnetic state are shown in Fig. 4. As shown in Fig. 4(a), there are four Fermi surface sheets, contributed from the four bands crossing the Fermi energy [Fig. 4(a)]. Among them, the two cylinder-like Fermi-surface sheets centered around X–P are from the electron bands. They correspond to the two Fermi surface sheets around M–A in LaFeAsO. The other two Fermi surface sheets centered around Γ–Z are from the hole bands. These results agree qualitatively with the

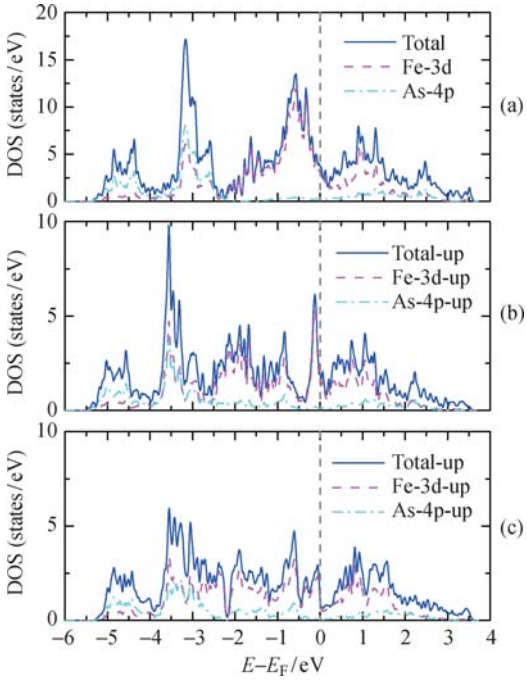

Fig. 2 Total and orbital-resolved partial density of states of $BaFe_2As_2$ per formula unit in **(a)** nonmagnetic state; **(b)** square antiferromagnetic Neel state with spin-up (the same for the spin-down); and **(c)** collinear antiferromagnetic state with spin-up (the same for the spin-down), respectively.

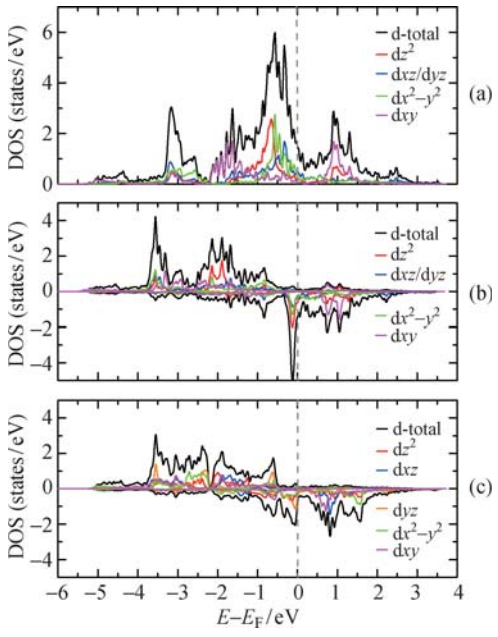

Fig. 3 Total and projected density of states at the five Fe-3d orbitals of $BaFe_2As_2$ per Fe atom in **(a)** nonmagnetic state, **(b)** square antiferromagnetic Neel state, and **(c)** collinear antiferromagnetic state, respectively.

experimental observation [20].

The energy dispersion of the electronic bands along the c-axis is much larger than that in LaFeAsO [21, 22]. The sectional views parallel to (001) plane through Z point and Γ point are different due to the large dispersion [Figs. 4(c) and (d)]. There is one band just below the Fermi energy along Γ–Z in Fig. 4(a), which corresponds to the third hole Fermi surface sheet given in Ref. [14]. The volumes enclosed by these Fermi surface sheets are 0.26 electrons/cell and 0.26 holes/cell, respectively. The electron carrier concentration is the same as the hole carrier concentration. Both are equal to $2.54 \times 10^{21}/\mathrm{cm}^3$. The compound $BaFe_2As_2$ is thus a semimetal with a low carrier concentration between normal metals and semiconductors, similar to what we found in LaFeAsO [22]. The density of states at the Fermi energy is 3.93 state per eV per formula unit cell. The corresponding electronic specific heat coefficient $\gamma = 9.26\ \mathrm{mJ/(K^2 \cdot mol)}$ and the Pauli paramagnetic susceptibility $\chi_p = 1.60 \times 10^{-9}\ \mathrm{m^3/mol}$. These calculated physical quantities are also summarized in Table 1, which are well close to the experimental values [9, 23–26].

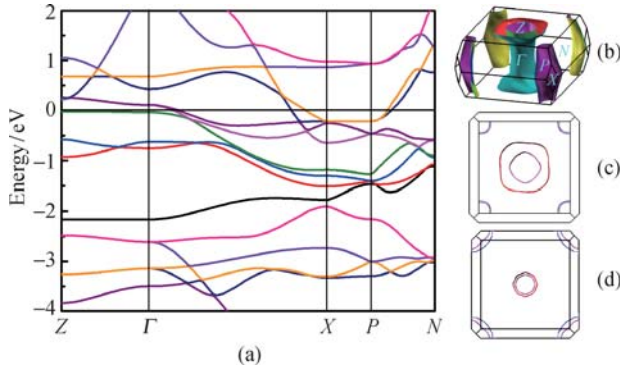

Fig. 4 **(a)** Electronic band structure of $BaFe_2As_2$ in a primitive unit cell for the nonmagnetic state. The Fermi surface **(b)** and its sectional views through symmetrical k-point Z **(c)** and Γ **(d)** parallel to (001) plane.

We study the plasma excitation in the semimetal $BaFe_2As_2$ as well. The plasma frequency f_p is computed as follows:

$$f_p = \frac{1}{2\pi}\sqrt{4\pi e^2\left(\frac{n_h}{m_h^*} + \frac{n_e}{m_e^*}\right)} \tag{1}$$

where n_h and n_e are the hole and electron carrier densities, respectively and m_h^* and m_e^* are the effective masses of hole and electron, respectively. We use the second order polynomial fitting to estimate the effective masses of carriers from the calculated band structures. We obtain the hole and electron effective masses as $m_e^* = 0.60m_e$ and $m_h^* = 0.86m_e$ with m_e being electron mass. Because of the irregular and strongly anisotropic band structure, the estimated effective masses are with no small uncertainty. We then calculate the plasma frequency as $f_p = 25\ 392\ \mathrm{cm}^{-1}$ in the nonmagnetic state. These values are also listed in Table 1 in comparison with the available experimental values.

3.1.2 $SrFe_2As_2$

Like $BaFe_2As_2$, $SrFe_2As_2$ can also become superconduct-

Table 1 Calculated (Cal.) physical quantities in comparison with the available experimental (Exp.) values for AFe$_2$As$_2$ (A=Ba, Sr, or Ca) in the nonmagnetic state (NM) and the collinear antiferromagnetic state (Col). The units for the carrier density ρ, the plasma frequency f_p, the electronic specific heat coefficient γ, and the Pauli paramagnetic susceptibility χ_p are 10^{21}/cm^3, cm^{-1}, mJ/(K$^2\cdot$mol), and 10^{-9} m^3/mol, respectively. J_1 and J_2 (meV/S^2 per Fe) are the superexchange antiferromagnetic couplings between the nearest and the next nearest neighbor Fe spins $\boldsymbol{S}$ in ab-plane, respectively while J_z (meV/S^2 per Fe) is the interlayer superexchange antiferromagnetic coupling of Fe spins $\boldsymbol{S}$ perpendicular to ab-plane.

AFe$_2$As$_2$	State	ρ		f_p		γ		χ_p	Coupling		
		Hole	Electron	Cal.	Exp.	Cal.	Exp.		J_1	J_2	J_z
BaFe$_2$As$_2$	NM	2.54	2.54	25392	12900 [27]	9.26	37 [28], 16 [9],	1.60	25.5	33.8	3.1
	Col	0.10	0.21	7717	4660 [27]	5.68	6.1 [23]				
SrFe$_2$As$_2$	NM	3.33	3.33	27386	13840 [27]	7.71	6.5	1.33	14.7	33.4	7.8
	Col	0.13	0.04	4249	4750 [27]	3.63					
CaFe$_2$As$_2$	NM	4.21	4.21	20883		9.31	8.2	1.60	–1.4	26.8	14.8
	Col	0.09	0.09	5557		2.62					

ing by chemical doping or by applying a high pressure. These two compounds have the same crystal structure. The tetragonal crystal lattice constants determined by experimental measurements are $a = b = 3.9259$ Å and $c = 12.375$ Å for SrFe$_2$As$_2$ [4]. They are smaller than the corresponding parameters for BaFe$_2$As$_2$, especially along the c-axis. The electronic band structure and the Fermi surface shown in Fig. 5, are similar as the ones for BaFe$_2$As$_2$. The difference is that the band along Γ–Z, which is just below the Fermi energy in BaFe$_2$As$_2$, moves slightly upward and intersects with the Fermi level. This results in the third hole-type Fermi sheet centered around Γ–Z. Therefore, in SrFe$_2$As$_2$, there are three hole-type and two electron-type Fermi surface sheets.

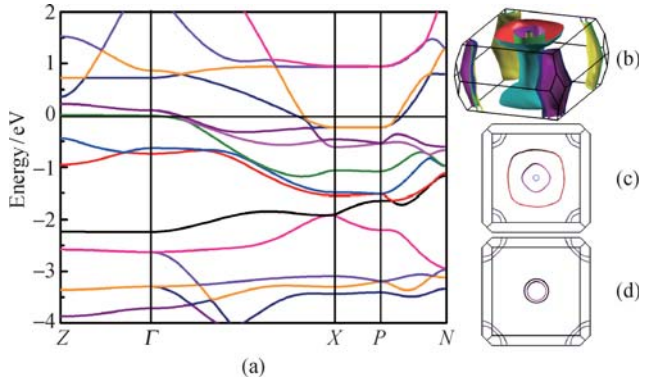

Fig. 5 Calculated electronic structure of SrFe$_2$As$_2$ in a primitive unit cell for the nonmagnetic state. **(a)** Electronic band structure; The Fermi surface **(b)** and its sectional views through symmetrical k-point Z **(c)** and Γ **(d)** parallel to (001) plane. The symmetrical k-points in the Brillouin zone are referred to Fig. 4(b).

The volumes enclosed by these Fermi sheets give 0.32 electrons/cell and 0.32 holes/cell for SrFe$_2$As$_2$. The electron (or hole) carrier concentration is about 3.33×10^{21}/cm^3. The density of states at the Fermi energy is about 3.27 state per eV per formula unit. The corresponding electronic specific heat coefficient and Pauli susceptibility are $\gamma = 7.71$ mJ/(K$^2\cdot$ mol) and $\chi_p = 1.33\times10^{-9}$m^3/mol, respectively. And the plasma frequency f_p is computed as about 27 386 cm^{-1}. These calculated quantities are also reported in Table 1. The total and Fe-3d projected density of states of SrFe$_2$As$_2$ are similar as the ones for BaFe$_2$As$_2$. The low energy excitations are also dominated by Fe-3d orbitals from −2 eV to 2 eV around the Fermi energy.

3.1.3 *CaFe$_2$As$_2$*

The tetragonal crystal lattice parameters obtained by experiments [26], $a = b = 3.912$ Å and $c = 11.667$ Å, are used in our calculation for CaFe$_2$As$_2$. Figure 6 shows the electronic band structure and the Fermi surface. Similar to SrFe$_2$As$_2$, there are three hole-type and two electron-type Fermi surface sheets for CaFe$_2$As$_2$. Because the third hole-type Fermi surface of CaFe$_2$As$_2$ expands into a cylinder-like shape centered around Γ–Z, the cross section through Γ and X in (001) plane has one more cutting line than that of SrFe$_2$As$_2$. From the volumes enclosed by these Fermi sheets, we determine the electron and hole concentrations are 0.38 electrons/cell and 0.38 holes/cell, respectively. The corresponding electron (or hole) carrier density is about 4.21×10^{21}/cm^3. The density of states at the Fermi energy is 3.95 state per eV per formula unit, and the electronic specific heat coefficient γ

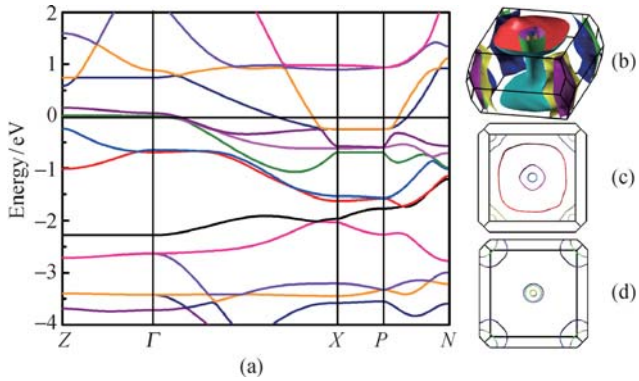

Fig. 6 Calculated band structure and Fermi surface of CaFe$_2$As$_2$ in a primitive unit cell for the nonmagnetic state. **(a)** Electronic band structure; **(b)** Fermi surface; And the sectional views through symmetrical k-point Z **(c)** and Γ **(d)** parallel to (001) plane. The symmetrical k-points in the Brillouin zone are referred to Fig. 4(b).

$= 9.31$ mJ/(K^2·mol) and Pauli paramagnetic susceptibility $\chi_p = 1.60 \times 10^{-9}$m^3/mol. And the plasma frequency f_p is computed as about 20883 cm^{-1}. These calculated quantities are summarized in Table 1. The total and Fe-3d orbital projected density of states of $CaFe_2As_2$ are almost the same as the ones for $SrFe_2As_2$.

3.2 Antiferromagnetic Neel state

To study the electronic structures of AFe_2As_2 in a magnetic state, we break the spin up-down symmetry by assigning a finite magnetic moment to each Fe atom. The ferromagnetic state is found to be not stable in AFe_2As_2, similar as in LaFeAsO [22]. However, the antiferromagnetic Neel state is meta-stable. Its energy is lower than the corresponding nonmagnetic state by 0.232 eV, 0.175 eV, and 0.133 eV per formula unit for $BaFe_2As_2$, $SrFe_2As_2$, and $CaFe_2As_2$, respectively. The magnetic moments in $BaFe_2As_2$, $SrFe_2As_2$, and $CaFe_2As_2$ are found to be respectively 2.3 μ_B/Fe, 2.2 μ_B/Fe, and 2.0 μ_B/Fe, similar as the one for LaFeAsO [22], while a moment of about 1.7 μ_B/Fe was found for all these three systems in the full potential local-density approximation calculations [29]. The density of states for the antiferromagnetic Neel state of $BaFe_2As_2$ is shown in Figs. 2(b) and 3(b). The corresponding electronic band structure with the Fermi surface shapes is shown in Fig. 7. The electronic structures and the Fermi surface topology are similar for the other two ternary iron arsenides in the antiferromagnetic Neel state.

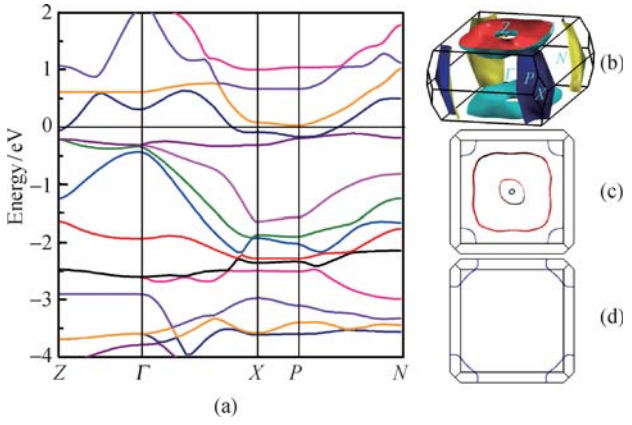

Fig. 7 The electronic structure of $BaFe_2As_2$ in a primitive unit cell for the metastable square antiferromagnetic Neel state. **(a)** Electronic band structure; The Fermi surface **(b)** and its the sectional views through symmetrical k-point Z **(c)** and Γ **(d)** parallel to (001) plane.

As shown in Fig. 2(b), the density of states around there is substantially reduced around -0.5 eV in comparison with that in the nonmagnetic state [Fig. 2(a)]. The missing states are pushed down to around -2.0 eV. This change can be also seen by comparing the electronic band structures of the nonmagnetic and the square antiferromagnetic Neel states, shown in Fig. 4(a) and Fig. 7(a). In contrast to the nonmagnetic state, there are only two bands crossing the Fermi energy, forming a ring-like hole-type shape around Z, a cylinder-like electron-type sheet centered around X–P, and a small-pocket-like electron-type sheet around Z.

3.3 Collinear antiferromagnetic state

For $BaFe_2As_2$, $SrFe_2As_2$, and $CaFe_2As_2$, the antiferromagnetic Neel state is a meta-stable state among the rich magnetic structures. It is found that the true ground state is in fact a collinear antiferromagnetic state with the interlayer Fe moments in antiferromagnetic alignment. The spin configuration of this state in FeAs layer is schematically shown in Fig. 1(c).

3.3.1 $BaFe_2As_2$

For $BaFe_2As_2$, the energy of the collinear antiferromagnetic state is lowered by 0.400 eV per formula unit than that of the nonmagnetic state. The magnetic moment is found to be about $2.65\mu_B$ for each Fe ion in this state. The electronic band structure and the density of states are shown in Fig. 8(a) and Fig. 2(c), respectively. In contrast to the nonmagnetic state, the density of states of As 4p orbitals in the low energy range from -2 eV to 0 eV is substantially enhanced in the collinear antiferromagnetic state.

Figure 8(c) shows the Fermi surface shapes of $BaFe_2As_2$ in the collinear antiferromagnetic state. There are two bands crossing the Fermi level. They lead to a hole-type Fermi surface and an electron-type Fermi surface, respectively. Here, we remind that if we consider $BaFe_2As_2$ by a tetragonal unit cell, the axis MA in the Brillouin zone of the tetragonal unit cell is now folded into the ΓZ, in which M point coincides with Γ point. This means that the electron-type Fermi sheet around M point in the tetragonal unit cell in the nonmagnetic state will be gapped when the collinear antiferromagnetic order takes place. From the volumes enclosed by these two

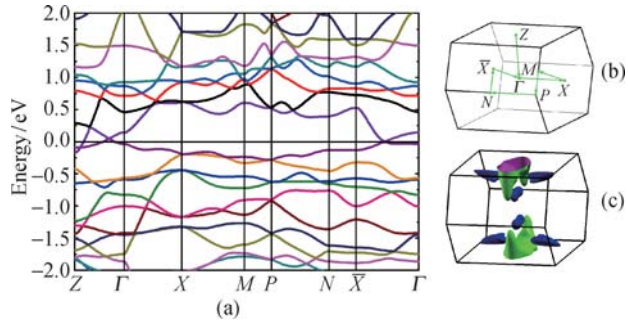

Fig. 8 Calculated band structure and Fermi surface of $BaFe_2As_2$ in the collinear antiferromagnetic state with the antiparallel alignment between the interlayer Fe moments along c-axis [30], which is the ground state. **(a)** Electronic band structure; **(b)** Brillouin zone; **(c)** Fermi surface.

Fermi sheets, we find that the electron carrier concentration is 0.042 electrons/cell, namely $2.05 \times 10^{20}/\mathrm{cm}^3$. The corresponding hole carrier concentration is 0.021 holes/cell, namely $1.03 \times 10^{20}/\mathrm{cm}^3$. Thus the electron concentration dominates over the hole concentration, unlike in the nonmagnetic state. By using the second-order polynomial to fit the calculated band structures, we estimate the electron effective masses as $m_e^* = 0.31m_e$ with m_e being electron mass. We then calculate the plasma frequency as $f_p = 7717\ \mathrm{cm}^{-1}$. Here the contribution of the holes to the plasma frequency is negligible. These values are also listed in Table 1 in comparison with the available experimental values.

In comparison with the nonmagnetic state, the electron effective mass becomes much lighter. Meanwhile, the carrier density is reduced by an order of magnitude, as shown in Table 1. This reduction is significantly smaller than that in LaFeAsO. In LaFeAsO, the carrier density is reduced by two orders of magnitude in the collinear antiferromagnetic state than in the nonmagnetic state [19]. The density of states at the Fermi energy E_F is 2.41 state per eV per formula unit cell. From this, we find that the electronic specific heat coefficient $\gamma = 5.68\ \mathrm{mJ/(K^2 \cdot mol)}$. It should be emphasized that the calculated value of γ in the collinear antiferromagnetic state should be smaller than the intrinsic value of γ at zero temperature measured by experiments since the low energy quantum spin fluctuations are suppressed in the calculations, as discussed in Section 4. Therefore, the measured γ in the low temperature limit should be bound between the two calculated γ values obtained by our calculations for the nonmagnetic and collinear antiferromagntic states, respectively. In Table 1, we compare the calculated specific heat coefficients γ with the corresponding experimental values. For $BaFe_2As_2$, there is a large variety in the measurement values. Experimentally, the first reported measurement value of γ is about $37\ \mathrm{mJ/(K^2 \cdot mol)}$ [28], much larger than our DFT result. However, with the sample quality being improved, the second reported value of γ becomes $16\ \mathrm{mJ/(K^2 \cdot mol)}$ [9]; and the latest reported value of γ is $6.1\ \mathrm{mJ/(K^2 \cdot mol)}$ [23], which is in fact good consistent with our DFT calculation. For $SrFe_2As_2$ and $CaFe_2As_2$, our calculated results are also consistent with the measurement values.

In the collinear antiferromagnetic state, there is further a small energy gain if the Fe-Fe distance is reduced along the spin parallel alignment direction and expanded along the spin anti-parallel alignment direction. This leads to a structural transition from tetragonal space group $I4/mmm$ to orthorhombic space group $Fmmm$, similar to that in LaFeAsO [19] and observed by the neutron scattering [10]. This lattice relaxation is energetically favorable because the direct ferromagnetic exchange favors a shorter Fe–Fe separation while the antiferromagnetic superexchange favors a larger Fe–As–Fe angle. It turns out that the angle γ in ab-plane is no longer rectangular [Fig. 1(c)] and the energy gain is 3 meV per formula unit, when γ is about 90.8°, similar as in LaFeAsO [19]. The correction from this lattice distortion to the electronic band structure as well as the Fe moments is very small.

Along the c-axis, we find that the Fe-spins between the nearest neighbor FeAs layers interact antiferromagnetically and the energy gain by taking the anti-parallel alignment is about 0.012 eV per formula unit cell in comparison with the parallel alignment. This antiferromagnetic interaction between the nearest neighboring FeAs layers is significantly larger than that in LaFeAsO [19]. In Ref. [1], we reported the electronic band structure and the Fermi surface of $A\mathrm{Fe_2As_2}$ (A=Ba, Sr, Ca) in the collinear antiferromagnetic order with the parallel alignment along the c-axis.

3.3.2 $SrFe_2As_2$

For $SrFe_2As_2$, the energy of the collinear antiferromagnetic state is lowered by 0.383 eV per formula unit than the one of the nonmagnetic state. The magnetic moment is about $2.55\mu_\mathrm{B}$ per Fe atom. The electronic band structure and the Fermi surface are shown in Fig. 9. From the volumes enclosed by the Fermi surface sheets, we find that the electron and hole carrier concentrations are about 0.008 electrons/cell and 0.025 holes/cell, namely about $0.44 \times 10^{20}/\mathrm{cm}^3$ and $1.31 \times 10^{20}/\mathrm{cm}^3$, respectively. It turns out that the hole concentration dominates over the electron concentration, unlike the case of $BaFe_2As_2$. And the plasma frequency f_p is computed as about $4249\ \mathrm{cm}^{-1}$. In comparison with the nonmagnetic state, the carrier density is much reduced, by more than an order of magnitude. The density of states at the Fermi energy E_F is 1.54 state per eV per formula unit cell, and the electronic specific heat coefficient $\gamma =$

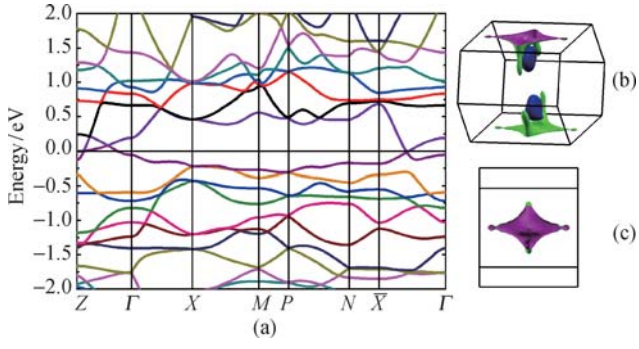

Fig. 9 Calculated band structure and Fermi surface of $SrFe_2As_2$ in the collinear antiferromagnetic state with the antiparallel alignment between the interlayer Fe moments along c-axis [30]. **(a)** Electronic band structure; **(b)** Side view: Fermi surface; **(c)** Top view: Fermi surface. The symmetrical k-points in the Brillouin zone are referred to Fig. 8(b).

3.63 mJ/(K^2 · mol). These calculated quantities are also reported in Table 1.

3.3.3 $CaFe_2As_2$

For $CaFe_2As_2$, the collinear antiferromagnetic ordering can lower the ground state energy by 0.352 eV per formula unit in comparison with the nonmagnetic state. There are about 2.49μ_B moment around each Fe atom. The electronic band structure and the Fermi surface are shown in Fig. 10. The electron (hole) carrier density is about 0.016 electrons/cell (0.016 holes/cell), or 0.90×10^{20}/cm^3 (0.90×10^{20}/cm^3). Thus, the electron concentration and the hole concentration are in balance, different from the ones in $BaFe_2As_2$ and $SrFe_2As_2$. And the plasma frequency f_p is computed as about 5557 cm^{-1}. Similar to $SrFe_2As_2$, the carrier density is also much reduced by more than an order of magnitude in comparison with the nonmagnetic state. The density of states at the Fermi energy E_F is about 1.11 state per eV per formula unit cell and the electronic specific heat coefficient $\gamma = 2.62$ mJ/(K^2 · mol). These calculated quantities are also reported in Table 1.

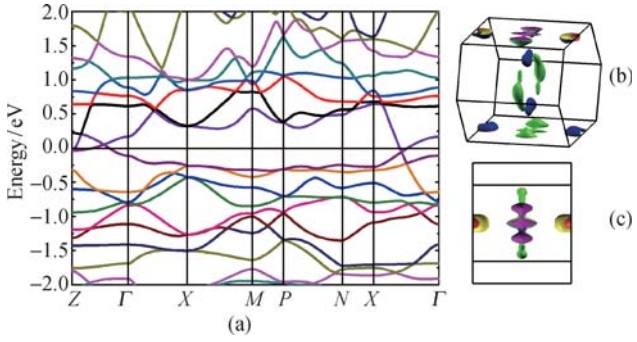

Fig. 10 Calculated band structure and Fermi surface of $CaFe_2As_2$ in the collinear antiferromagnetic state with the antiparallel alignment between the interlayer Fe moments along c-axis [30]. **(a)** Electronic band structure; **(b)** Side view: Fermi suface; **(c)** Top view: Fermi surface. The symmetrical k-points in the Brillouin zone are referred to Fig. 8(b).

3.4 Spin-orbit interaction

The spin-orbit interaction results from the relativistic effect. It is known that this interaction leads to many interesting features in transition metal oxides. To study how strong this interaction can affect the electronic properties of these materials, we performed a relativistic calculation for $BaFe_2As_2$. Figure 11 shows the electronic band structures of $BaFe_2As_2$ by including spin-orbit interaction in the nonmagnetic state. By comparison with Figs. 4(a) and 8(a), we find that the spin-orbit interaction splits the band mainly along Γ–Z into two bands by about 50–150 meV around the Fermi energy.

3.5 Pressure effect

Experimentally it was reported [11–13] that the ternary iron arsenides AFe_2As_2 (A=Ba, Ca, or Sr) can become superconducting under high pressures without doping. This provides another route to study the salient features of these materials in connection with the intrinsic electronic structures and properties. The superconducting phase appears when the pressure is in the ranges of 2.5–8, 28–37, and 22–58 kbar for $CaFe_2As_2$, $SrFe_2As_2$, and $BaFe_2As_2$ respectively. The highest superconducting transition temperatures for these three compounds are 12 K, 27 K, and 29 K, respectively.

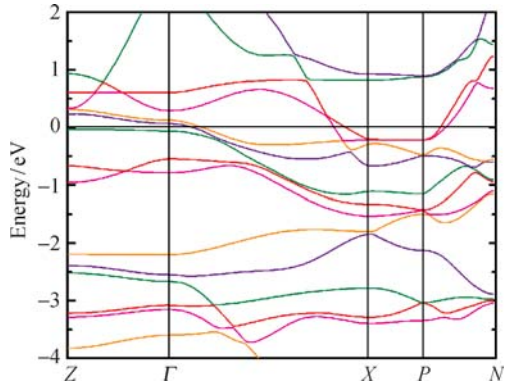

Fig. 11 Electronic band structures of $BaFe_2As_2$ including spin-orbit interaction in the nonmagnetic state.

Figure 12(a) shows the pressure dependence of relative energies for the nonmagnetic, square antiferromagnetic Neel and collinear antiferromagnetic states of $BaFe_2As_2$, respectively. The collinear antiferromagnetic state is robust against the pressure and has the lowest energy in the pressure range studied, consistent with the result reported in Ref. [31]. Note that in this calculation, the lattice parameters are relaxed when the pressure is zero. Thus, the energy differences are slightly different from that given before.

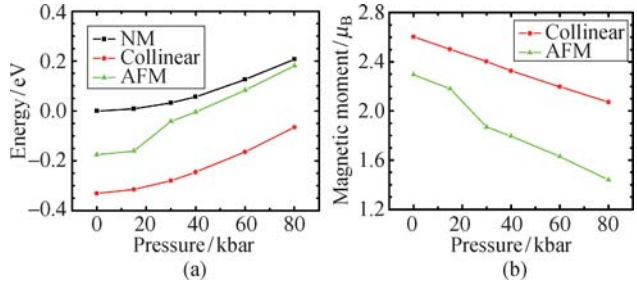

Fig. 12 **(a)** Calculated energy differences of $BaFe_2As_2$ between the magnetic state and the nonmagnetic state (NM) per formula unit cell under various pressures. Note the energy of the nonmagnetic state without pressure is set to zero. **(b)** The magnetic moments for the collinear antiferromagnetic state (Collinear) and the antiferromagnetic state (AFM) under the pressures.

The lattice structure of FeAs layers, including the angle between Fe and As atoms and the bond lengths of Fe–Fe, Fe–As, and As–As, is hardly changed by the pressure from 0 to 80 kbar. However, the contraction along the c axis is much more pronounced, especially in the nonmagnetic state. This indicates that the distance between the

neighboring FeAs and Ba layers is substantially reduced by pressure. This can strengthen the coupling between the neighboring FeAs layers and stabilize the long range antiferromagnetic correlation in the FeAs layer.

The magnetic moment in the magnetic states decreases almost linearly with pressure, as shown in Fig. 12(b). In our calculations, the magnetic moment is always larger than $2\mu_B$ in the collinear antiferromagntic state. The superexchange interaction thus remains dominant when a pressure is imposed.

4 Effective model

4.1 Local moment versus itinerant electrons

Physically the moments of Fe ions result from the on-site Coulomb repulsion and the Hund's rule coupling of 3d orbitals. An isolated Fe ion in a 2+ valency has a spin $S = 2$ with a large magnetic moment of $4\mu_B$. In iron-pnictide semimetals, the effective moment of a Fe ion (in a 2+ valency) will be reduced by its hybridization with other atoms and by the Coulomb screening of itinerant electrons. However, it will remain finite if the Hund's rule coupling and the on-site Coulomb repulsion is strong enough in comparison with the hybridization and other screening effects, as we found in LaFeAsO [19].

In our calculations, by projecting the density of states onto the five 3d orbitals of Fe in the collinear antiferromagnetic state of $BaFe_2As_2$ [Fig. 3(c)], we find that the five 3d orbitals of Fe are almost completely filled by up-spin electrons and nearly half-filled by down-spin electrons in one of the two sublattices (or completely filled by down-spin electrons and half-filled by up-spin electrons in the other sublattice). This indicates that the crystal field splitting imposed by As atoms is very small and the Fe 3d-orbitals hybridize strongly with each other. We can see that this is a universal feature for all iron pnictides, as we first found in LaFeAsO [19]. The strong polarization of Fe magnetic moments is thus due to the Hund's rule coupling.

In low temperatures, the Fe moments will interact with each other to form an antiferromagnetic ordered state. These ordered magnetic moments have been observed by elastic neutron scattering and other experiments [7, 10]. However, they are not exactly the moments obtained by the DFT calculations, as we indicated first for LaFeAsO [19]. This is because the DFT calculation is done based on a small magnetic unit cell and the low-energy quantum spin fluctuations as well as their interactions with itinerant electrons are frozen by the finite excitation gap due to the finite-size effect. Thus, the moment obtained by the DFT is the bare moment of each Fe ion. It should be larger than the ordering moment measured by neutron scattering and other experiments. Our calculations show that the bare magnetic moment around each Fe atom is about 2.2–2.6 μ_B in all iron pnictides and in different magnetically ordered states.

In high temperatures, there is no net static moment in the paramagnetic phase due to the thermal fluctuation, but the bare moment of each Fe ion can still be measured by a fast local probe like ESR (electron spin resonance). Very recently, the bare moment of Fe has been observed in the paramagnetic phase by the ESR measurement [40]. The value of the moment detected by ESR is about 2.2–2.8 μ_B in good agreement with our DFT result, which is but significantly larger than the ordering moment in the antiferromagnetic phase.

Again similar to what we found in LaFeAsO [19], from the spatial distributions of electrons, we further find that there is a strong hybridization between neighboring Fe and As ions. This strong hybridization can mediate an antiferromagnetic superexchange interaction between the Fe moments. This superexchange interaction is antiferromagnetic since the intermediate state associated with the hopping bridged by As ions is a spin singlet. On the other hand, there is a relatively small but finite hybridization between two neighboring Fe ions. This direct hybridization of Fe 3d orbitals can induce a direct exchange interaction between the Fe moments. This direct exchange interaction is ferromagnetic due to the Hund's rule coupling. Furthermore, there is a strong covalent bonding or hybridization between As 4p orbitals although the separation between As atoms is relatively large. This hybridization gives rise to a broad As 4p band below the Fermi level. Thus, As 4p states are not truly localized. They form an electron network connecting As ions through covalent bonding, similar to what we found in iron chalcogenides (α-FeSe and α-FeTe) [32]. However, there is the difference that the band formed by As 4p-orbitals is insulating, as shown in Fig. 2, while the band formed by Te 5p orbitals is metallic (see Ref. [32]). It turns out that the exchange interaction bridged by As 4p orbitals is short ranged (just J_1 and J_2) while the one bridged by Te 5p orbitals can be long ranged, as we found in α-FeTe in which there is a substantial third nearest neighbor antiferromagnetic superexchange interaction J_3 besides J_1 and J_2 [32].

4.2 t–J_H–J_1–J_2 Hamiltonian

For iron-based pnictides, the low energy spin dynamics could be approximately described by an antiferromagnetic Heisenberg model with the nearest and the next-nearest neighbor exchange interactions. However, the Fe spin (or magnetic moment) is not quantized since the electrons constituting the moment can propagate on the lattice, like in hole or electron doped high T_c superconductivity cuprates. Besides these superexchange interactions, the on-site Hund's rule coupling among different

Fe 3d orbitals is important. This is because the crystal splitting of Fe 3d levels is very small and the spins of Fe 3d electrons are polarized mainly by this interaction. Thus, we believe that the low-energy physical properties of these iron-based pnictides can be approximately described by the following effective Hamiltonian

$$H = \sum_{\langle ij\rangle,\alpha\beta} t_{ij}^{\alpha\beta} c_{i\alpha}^{\dagger} c_{j\beta} - J_H \sum_{i,\alpha\neq\beta} \boldsymbol{S}_{i\alpha}\cdot\boldsymbol{S}_{i\beta} + J_1 \sum_{\langle ij\rangle,\alpha\beta} \boldsymbol{S}_{i\alpha}\cdot\boldsymbol{S}_{j\beta} + J_2 \sum_{\langle\langle ij\rangle\rangle,\alpha\beta} \boldsymbol{S}_{i\alpha}\cdot\boldsymbol{S}_{j\beta} \quad (2)$$

where $\langle ij\rangle$ and $\langle\langle ij\rangle\rangle$ represent the summation over the nearest and the next-nearest neighbors, respectively. α and β are the indices of Fe 3d orbitals. $c_{i\alpha}^{\dagger}$ ($c_{i\alpha}$) is the electron creation (annihilation) operator:

$$\boldsymbol{S}_{i\alpha} = c_{i\alpha}^{\dagger} \frac{\boldsymbol{\sigma}}{2} c_{i\alpha} \quad (3)$$

is the spin operator of the α orbital at site i. The total spin operator at site i is defined by $\boldsymbol{S}_i = \sum_\alpha \boldsymbol{S}_{i\alpha}$. In Eq. (2), J_H is the on-site Hund's coupling among the five Fe 3d orbitals. The value of J_H is generally believed to be about 1 eV. $t_{ij}^{\alpha\beta}$ are the effective hopping integrals that can be determined from the electronic band structure in the nonmagnetic state [33].

The nearest and the next-nearest neighbor antiferromagnetic coupling constants, J_1 and J_2, in Eq. (2) can be calculated from the relative energies of the ferromagnetic, square antiferromagnetic, and collinear antiferromagnetic states with respect to the non-magnetic state. For the corresponding detailed calculations, please refer to the appendix in our paper in Ref. [19]. For $BaFe_2As_2$, the energy of the ferromagnetic state is about 8meV per Fe lower than the nonmagnetic state and the Fe moment is about $2.3\mu_B$. From this and the relative energies of the two antiferromagnetic states, we find that the exchange constants are approximately given by J_1= 25.5 meV/S^2 per Fe and J_2 = 33.8 meV/S^2 per Fe (S is the spin of the Fe ion) for $BaFe_2As_2$. Meanwhile, we also find that the interlayer superexchange antiferromagnetic coupling J_z =3.1 meV/S^2 per Fe. In obtaining these values, we have assumed that the contribution of itinerant electrons to the energy is almost unchanged in different magnetically ordered states. Since the bare $t_{ij}^{\alpha\beta}$ and J_H can be considered independent of magnetic structures, the relative energies between different magnetic states are not affected by itinerant electrons. For $SrFe_2As_2$ and $CaFe_2As_2$, the values of J_1 and J_2 with J_z are determined as well and given in Table 1. As we notice, J_1 in $CaFe_2As_2$ is negative, namely ferromagnetic, which is unique among iron pnictides.

4.3 Discussion

We plot the superconducting critical temperatures T_c versus J_2 for these compounds with doping carriers or by applying high pressures in Fig. 13. Interesting, as we see, the maximum critical temperatures T_c are in proportion to the next-nearest neighbor superexchange interaction J_2. This suggests that there would exist an intrinsic relationship between the superconductivity and the As-bridged superexchange antiferromagnetic interactions. Here we have assumed that the value of J_2 does not change with doping or pressure in comparison with the ones of the parent compounds. This can be verified from Fig. 14. Figure 14 shows how the superexchange interactions J_1 and J_2 change with the pressure, from which we find that J_2 slightly changes with the pressure. However, J_1 drops quickly with increasing pressure. This is because the energy difference between the non-magnetic state and the square antiferromagnetic Neel state can be significantly reduced by the pressure, as shown in Fig. 12.

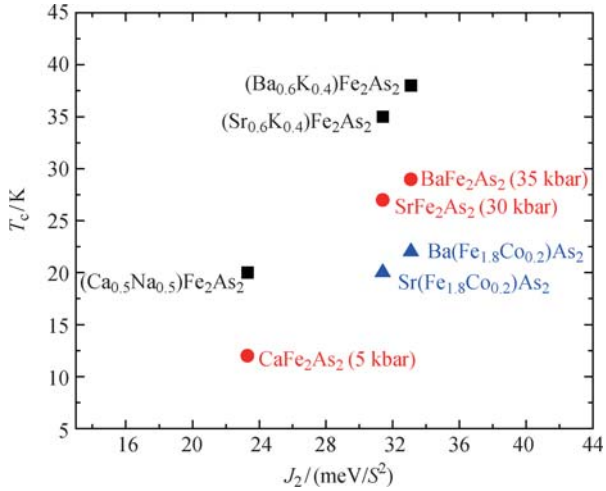

Fig. 13 Various critical superconductivity temperature T_c versus exchange interaction J_2 for AFe_2As_2 (A=Ba, Ca, or Sr) with doping or under high pressures. T_c are taken from Refs. [3, 5, 13, 25, 34, 35].

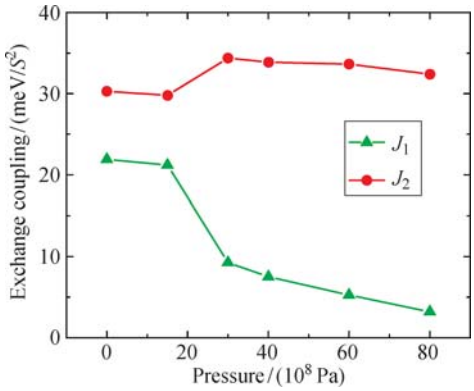

Fig. 14 Variations of superexchange antiferromagnetic interaction constants J_1 and J_2 with the imposed pressure for $BaFe_2As_2$.

In comparison with the bare $t_{ij}^{\alpha\beta}$ and J_H, J_1 and J_2 are very small. When we study charge dynamics like charge transport happening in iron pnictides, $t_{ij}^{\alpha\beta}$-J_H part will

thus play a dominant role. In Eq. (2), if the J_1 and J_2 terms are ignored, the Hamiltonian will look similar to the double exchange model that was proposed for describing the physical properties of colossal magnetoresistance (CMR) of manganese oxides [36, 37]. However, there is an essential difference. In manganese oxides the crystal field splitting between e_g and t_{2g} orbitals is very large, the moments polarized by the Hund's rule coupling on the t_{2g} orbitals are completely localized and only e_g electrons can hop on the lattice. In contrast, in iron pnictides, all five 3d orbitals of Fe have contributions to the moment and at the same time they can also hop on the lattice. Nevertheless, we believe that their charge dynamics share a common feature. In manganese oxides there is a strong spin-dependent scattering on the conduction electrons due to the strong Hund's coupling between e_g and t_{2g} levels of Mn ions. If the localized core spins of Mn are aligned ferromagnetically, the scattering of the electrons due to the core spins will be dramatically reduced because of no spin-flip, leading to a giant magneto-resistance and a sharp drop of resistivity with decreasing temperature in the ferromagnetic phase. In iron pnictides, there is also a strong spin-dependent scattering on conduction electrons caused by the Hund's rule coupling. In low temperatures, the moments of Fe ions are in the collinear antiferromagnetic order, in which the Fe moments are aligned antiferromagnetically along one direction but ferromagnetically along the other direction perpendicular. Similar as in manganese oxides, the scattering of electrons along the ferromagnetic direction is significantly reduced, leading to a sharp drop of resistivity and a large magneto-resistivity in the collinear antiferromagnetic phase, in agreement with experimental measurements [25, 38].

5 Conclusion

In conclusion, we have reported calculated results on the electronic band structures of $A\mathrm{Fe_2As_2}$ (A=Ba, Ca, or Sr) by using the first-principles electronic structure calculations. The ground state of $\mathrm{AFe_2As_2}$ is shown to be a collinear antiferromagnetic semimetal with a large magnetic moment around each Fe ion. The electronic structure is weakly affected by the spin-orbit interaction, but strongly altered by pressure. We have determined the density of states at the Fermi level, the specific heat coefficient and the Pauli susceptibility in both the nonmagnetic and collinear antiferromagnetic states. The effective antiferromagnetic coupling constants of the Fe moments are also estimated assuming that the low-energy spin dynamics is approximately described by the Heisenberg model with the nearest and the next-nearest neighboring exchange terms. Based on the analysis of electronic and magnetic structures, we proposed that the low-energy physics of $\mathrm{AFe_2As_2}$ can be effectively described by the t–J_H–J_1–J_2 model, defined by Eq. (2).

Acknowledgements This work was partially supported by the National Natural Science Foundation of China and the National Program for Basic Research of Ministry of Science and Technology, China.

References

1. Part of the calculations presented in this paper had been first reported in our paper, arXiv: 0806.3526v2, 2008
2. Y. Kamihara, T. Watanabe, M. Hirano, and H. Hosono, J. Am. Chem. Soc., 2008, 130: 3296
3. M. Rotter, M. Tegel, and D. Johrendt, Phys. Rev. Lett., 2008, 101: 107006
4. K. Sasmal, B. Lv, B. Lorenz, A. Guloy, F. Chen, Y. Xue, and C. W. Chu, Phys. Rev. Lett., 2008, 101: 107007
5. G. Wu, H. Chen, T. Wu, Y. L. Xie, Y. J. Yan, R. H. Liu, X. F. Wang, J. J. Ying, and X. H. Chen, J. Phys.: Condens. Matter, 2008, 20: 422201
6. M. C. Boyer, K. Chatterjee, W. D. Wise, G. F. Chen, J. L. Luo, N. L. Wang, and E. W. Hudson, arXiv: 0806.4400, 2008
7. C. de la Cruz, Q. Huang, J. W. Lynn, J. Li, W. Ratcliff, J. L. Zarestky, H. A. Mook, G. F. Chen, J. L. Luo, N. L. Wang, and P. Dai, Nature, 2008, 453: 899
8. M. A. McGuire, A. D. Christianson, A. S. Sefat, R. Jin, E. A. Payzant, B. C. Sales, M. D. Lumsden, and D. Mandrus, Phys. Rev. B, 2008, 78: 094517
9. M. Rotter, M. Tegel, I. Schellenberg, W. Hermes, R. Pöttgen, and D. Johrendt, Phys. Rev. B, 2008, 78: 020503(R)
10. Q. Huang, Y. Qiu, W. Bao, J. W. Lynn, M. A. Green, Y. C. Gasparovic, T. Wu, G. Wu, and X. H. Chen, Phys. Rev. Lett., 2008, 101: 257003
11. M. S. Torikachvili, S. L. Bud'ko, N. Ni, and P. C. Canfield, Phys. Rev. Lett., 2008, 101: 057006
12. T. Park, E. Park, H. Lee, T. Klimczuk, E. D. Bauer, F. Ronning, and J. D. Thompson, J. Phys.: Condens. Matter, 2008, 20: 322204
13. P. L. Alireza, J. Gillett, Y. T. C. Ko, S. E. Sebastian, and G. G. Lonzarich, J. Phys.: Condens. Matter, 2009, 21: 012208
14. I. A. Nekrasov, Z. V. Pchelkina, and M. V. Sadovskii, JETP Letters, 2008, 88: 144
15. D. J. Singh, Phys. Rev. B, 2008, 78: 094511
16. P. Giannozzi, et al., http://www.quantum-espresso.org
17. J. P. Perdew, K. Burke, and M. Ernzerhof, Phys. Rev. Lett., 1996, 77: 3865
18. D. Vanderbilt, Phys. Rev. B, 1990, 41: 7892
19. F. Ma, Z. Y. Lu, and T. Xiang, Phys. Rev. B, 2008, 78: 224517
20. L. X. Yang, Y. Zhang, H. W. Ou, J. F. Zhao, D. W. Shen, B. Zhou, J. Wei, F. Chen, M. Xu, C. He, Y. Chen, Z. D. Wang, X. F. Wang, T. Wu, G. Wu, X. H. Chen, M. Arita, K. Shimada, M. Taniguchi, Z. Y. Lu, T. Xiang, and D. L. Feng, Phys. Rev. Lett., 2009, 102: 107002
21. D. J. Singh and M. H. Du, Phys. Rev. Lett., 2008, 100:

237003
22. F. Ma and Z. Y. Lu, Phys. Rev. B, 2008, 78: 033111
23. J. K. Dong, L. Ding, H. Wang, X. F. Wang, T. Wu, G. Wu, X. H. Chen, and S. Y. Li, New Journal of Physics, 2008, 10: 123031
24. F. Ronning, T. Klimczuk, E. D. Bauer, H. Volz, and J. D. Thompson, J. Phys.: Condens. Matter, 2008, 20: 322201
25. G. F. Chen, Z. Li, J. Dong, G. Li, W. Z. Hu, X. D. Zhang, X. H. Song, P. Zheng, N. L. Wang, and J. L. Luo, Phys. Rev. B, 2008, 78: 224512
26. N. Ni, S. Nandi, A. Kreyssig, A. I. Goldman, E. D. Mun, S. L. Bud'ko, and P. C. Canfield, Phys. Rev. B, 2008, 78: 014523
27. W. Z. Hu, J. Dong, G. Li, Z. Li, P. Zheng, G. F. Chen, J. L. Luo, and N. L. Wang, Phys. Rev. Lett., 2008, 101: 257005
28. N. Ni, S. L. Bud'ko, A. Kreyssig, S. Nandi, G. E. Rustan, A. I. Goldman, S. Gupta, J. D. Corbett, A. Kracher, and P. C. Canfield, Phys. Rev. B, 2008, 78: 014507
29. C. Krellner, N. Caroca-Canales, A. Jesche, H. Rosner, A. Ormeci, and C. Geibel, Phys. Rev. B, 2008, 78: 100504
30. In Ref. [1], we had reported the electronic band structure and the Fermi surface of AFe$_2$As$_2$ (A=Ba, Sr, Ca) in the collinear antiferromagnetic order with the parallel alignment between interlayer Fe moments along c-axis.
31. W. H. Xie, M. L. Bao, Z. J. Zhao, and B. G. Liu, Phys. Rev. B, 2009, 79: 115128
32. F. Ma, W. Ji, J. P. Hu, Z. Y. Lu, and T. Xiang, Phys. Rev. Lett., 2009, 102: 177003
33. C. Cao, P. J. Hirschfeld, and H. P. Cheng, Phys. Rev. B, 2008, 77: 220506(R)
34. A. Leithe-Jasper, W. Schnelle, C. Geibel, and H. Rosner, 2008, arXiv: 0807.2223
35. A. S. Sefat, R. Jin, M. A. McGuire, B. C. Sales, D. J. Singh, and D. Mandrus, Phys. Rev. Lett., 2008, 101: 117004
36. R. V. Helmolt, J. Wocker, B. Holzapfel, L. Schultz, and K. Samwer, Phys. Rev. Lett., 1993, 71: 2331
37. C. Zener, Phys. Rev., 1951, 82: 403
38. P. Cheng, H. Yang, Y. Jia, L. Fang, X. Zhu, G. Mu, and H. H. Wen, Phys. Rev. B, 2008, 78: 134508
39. G. F. Chen, Z. Li, J. Dong, G. Li, W. Z. Hu, X. D. Zhang, X. H. Song, P. Zheng, N. L. Wang, and J. L. Luo, Phys. Rev. B, 2008, 78: 224512
40. T. Wu, J. J. Ying, G. Wu, R. H. Liu, Y. He, H. Chen, X. F. Wang, Y. L. Xie, Y. J. Yan, and X. H. Chen, Phys. Rev. B, 2009, 79: 115121